

ORIGINAL RESEARCH ARTICLE

Data-driven prediction of strain fields in auxetic structures and non-contact validation with mechanoluminescence for structural health monitoring

Junheui Jo[†], Minwoo Park[†], Sukheon Kang[†], Hugon Lee[†],
Chang-Yeon Gu[†], Taek-Soo Kim[†], and Seunghwa Ryu^{*}

Department of Mechanical Engineering, Korea Advanced Institute of Science and Technology, Yuseong-gu, Daejeon, Republic of Korea

Abstract

Recent advancements in 3D printing technology have significantly enhanced the potential of auxetic structures, which are notable for their negative Poisson's ratio, particularly in applications such as sensor technology and structural health monitoring. Central to the performance of these structures is the accurate estimation of the effective strain parameter, a critical metric for assessing structural integrity. However, as structural complexity increases, estimating this parameter becomes increasingly challenging. The fabrication and real-world validation of these structures are equally important challenges. This paper introduces two key innovations for the practical application of auxetic structures. First, we present a multi-kernel hierarchical deep neural network that leverages finite element simulation data to accurately predict effective strain fields in complex auxetic configurations. This model architecture not only reduces the number of parameters requiring training but also enhances feature learning and generalization capabilities, achieving over 90% accuracy in predicting strain fields. Second, we validate these predictions using a 3D-printed specimen embedded with mechanoluminescent (ML) particles. This approach enables direct, non-contact visualization of strain in real-time, offering high spatial and temporal resolution. The alignment observed between predicted and observed strain concentration areas demonstrates the efficacy of integrating ML technology into auxetic designs. This integration significantly improves the reliability and diagnostic capabilities of advanced structural systems.

[†]These authors contributed equally to this work.

*Corresponding author:

Seunghwa Ryu
(ryush@kaist.ac.kr)

Citation: Jo J, Park M, Kang S, *et al.* Data-driven prediction of strain fields in auxetic structures and non-contact validation with mechanoluminescence for structural health monitoring. *Int J AI Mater Design*. 2024;1(2):48-60. doi:10.36922/ijamd.3539

Received: April 30, 2024

Accepted: June 18, 2024

Published Online: July 30, 2024

Copyright: © 2024 Author(s). This is an Open-Access article distributed under the terms of the Creative Commons Attribution License, permitting distribution, and reproduction in any medium, provided the original work is properly cited.

Publisher's Note: AccScience Publishing remains neutral with regard to jurisdictional claims in published maps and institutional affiliations.

Keywords: Mechanical metamaterials; Auxetic structure; Structural health monitoring; 3D printing; Mechanoluminescence; Deep learning

1. Introduction

Mechanical auxetic structures have gained significant attention in engineering applications, driven by advancements in additive manufacturing technologies that enable the production of complex shapes.¹⁻⁴ These structures exhibit a unique ability to expand laterally under tensile stress, characterized by a negative Poisson's ratio (NPR), which confers superior mechanical properties.^{5,6} Notably, auxetic structures are recognized for their enhanced shear resistance,

exceptional impact absorption, and augmented fracture resistance.⁷ They reduced the Poisson's ratio while amplifying strain sensitivity compared to conventional materials.^{8,9}

This heightened sensitivity is particularly pronounced in auxetic structures that leverage rotating motion under tensile stress to amplify their NPR behavior.^{10,11} Such sensitivity is, especially beneficial in fields such as structural health monitoring (SHM) and sensor technology, where precise monitoring of structural changes is crucial. However, the distinctive deformation responses of auxetic structures can lead to localized stress and strain concentrations, which must be addressed during the design process to prevent potential microcrack formation and failure over prolonged use. Hence, accurately measuring the spatial distribution of strain in both the design and application phases of auxetic materials is crucial.¹²⁻¹⁵

To evaluate deformation without causing material damage or alterations, non-contact methods have been developed to visualize strain fields. These methods encompass thermal,¹⁶ acoustic,^{17,18} optical,^{19,20} and luminescent²¹⁻²³ techniques, each offering distinct advantages and challenges. Among these, mechanoluminescence (ML) materials have emerged as a novel non-contact method. ML materials can visualize stress and strain fields and track crack paths in response to mechanical stimuli,^{24,25} offering the potential to map the spatial distribution of local mechanical responses.¹² Specifically, $\text{SrAl}_2\text{O}_4:\text{Eu}^{2+}, \text{Dy}^{3+}$ (SAOED), a representative material used in ML composites, demonstrates excellent reproducibility and a linear response to stress. This capability allows ML to provide strain distribution information comparable to traditional methods such as digital image correlation (DIC)²⁶ by quantifying light intensity without the use of speckle patterns.¹² Given the high costs and extensive pre-processing required for DIC setup and measurements, ML-aided evaluations of localized strains are expected to offer a cost-effective and deployable solution in SHM for various structures.

The predicted strain distribution from finite element analysis (FEA)²⁷⁻²⁹ and those derived from ML-based SHM methods can be effectively combined to enhance the design reliability of auxetic structures. With advancements in additive manufacturing, it is now possible to fabricate highly complex auxetic designs. However, the growing complexity of these structures, which encompass a vast design space, necessitates even more efficient prediction and design techniques. To meet these demands, recent developments have introduced artificial intelligence (AI). By integrating AI with FEA, various physical fields, such as stress fields, strain fields, and crack behaviors, as well as diverse design spaces, can be explored efficiently.³⁰⁻³³ Consequently, through the

analysis of physical fields, structural engineers can enhance mechanical properties by achieving more uniform stress distribution and reducing stress concentrations.

This study aims to leverage an AI-driven framework to predict effective strain within complex auxetic structures and employ ML materials to directly monitor strain fields. Auxetic designs incorporating ML were realized through 3D printing processes, and the predictive model's accuracy was validated by quantifying ML intensity. The observed linear relationship between ML intensity and effective strain, alongside comparisons with actual ML images, underscores the potential of 3D printing to produce complex auxetic structures embedded with ML particles for instantaneous verification of strain fields. Moreover, the application of ML in digital light processing (DLP)-based functional 3D printing demonstrates its broad potential across structural applications, confirming its feasibility for sensing and SHM. This research illustrates a comprehensive approach where prediction, fabrication, and direct verification of structural properties, focusing on the effective strain, are achievable simultaneously. It showcases the versatility and practical applicability of this innovative methodology in fields requiring acute sensitivity to deformation, such as civil engineering,³⁴ aerospace engineering,³⁵ and monitoring deformation in pipes and sacrificial layers.^{36,37}

2. Methods

2.1. Generation of auxetic structures

2.1.1. Parametrization and design of auxetic structures

In this study, we designed auxetic structures with NPR characteristics utilizing Bézier curves, which are parametric curves defined by a set of control points, offering continuous and smooth curves. The Bézier curves characterize the void domain within the unit cell of auxetic structures (Figure 1A) and are defined by Equation 1:

$$B(t) = \sum_{i=0}^n \binom{n}{i} (i-t)^{n-i} t^i P_i, \quad t \in [0,1], \quad (1)$$

Where t is a continuous value between 0 and 1, P_i is the set of control points, and denotes the binomial coefficient. We employed four control points ($n = 4$) to balance design capability and cost for exploring design variables.³⁸ For the design of a single closed curve, a total of eight Bézier curves were utilized, as shown in Figure 1B. These eight Bézier curves were comprised two symmetrical shifts of two curves generated in the first quadrant, satisfying C_1 and C_2 continuities.³⁹

Subsequently, unit cells were constructed by rotating and symmetrically shifting the generated closed Bézier

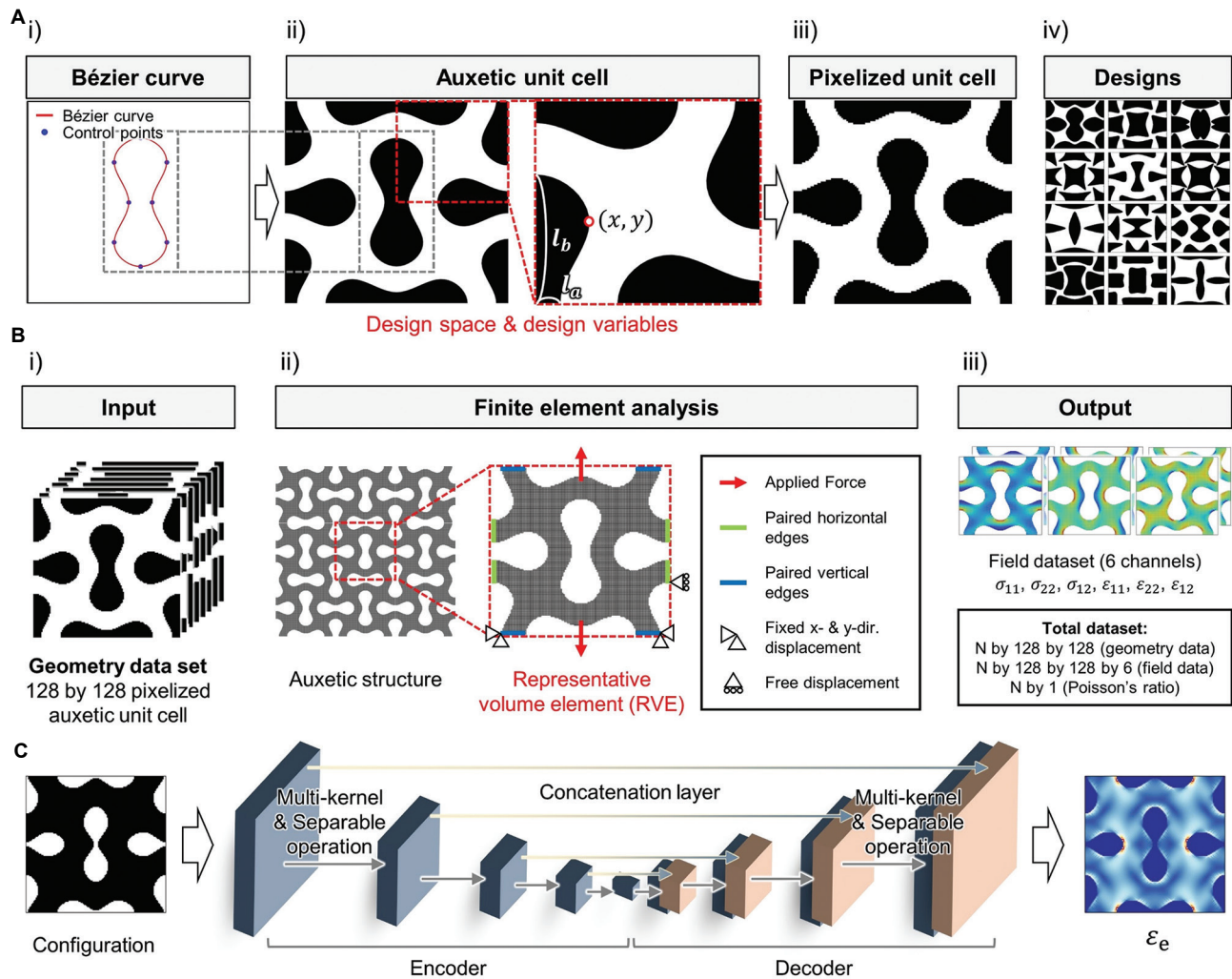


Figure 1. Design of auxetic structures, simulation data generation, and deep learning model architecture. (A) The design of auxetic unit cells: (i) closed Bézier curve design utilizing few sample points; (ii) designed auxetic unit cell from the Bézier curve with design variables; (iii) pixelized unit cell for data-driven study; and (iv) generated auxetic designs. (B) The data generation process: (i) 128 by 128 pixelized auxetic unit cell as input; (ii) Finite element analysis setup utilizing periodic boundary conditions for RVE; and (iii) simulation outputs consisting of three fields that are used to calculate the effective strain field. The dataset is configured as depicted, with N being the total number of designs. (C) The schematic of the modified MNet utilized in this study. The model has a backbone of U-Net with a multi-kernel dense block equipped with separable convolutional operations.

curves, defined by four design variables l_a , l_b , x , and y , as illustrated in Figure 1A(ii). The feasibility of generated designs was ensured by expressing the design variables in dimensionless form and assigning respective bounds as follows (Equations II, III, and IV):

$$\frac{1}{9} < \phi = \frac{l_a + l_b}{0.9L} \leq 1, \quad (II)$$

$$\frac{1}{9} < \tau = \frac{l_a}{l_b} < 1, \quad (III)$$

$$0.2 < x, y < 1, \quad (IV)$$

Where ϕ , τ , and (x, y) are defined as the thickness

ratio, aspect ratio, and shape parameters, respectively. After generating the unit cell design, it was pixelized into a 128×128 square grid for utilization in an image-based deep learning (DL) model, comprising convolutional neural networks (CNNs), as depicted in Figure 1A(iii). The design process was conducted using Matlab software (Matlab R2021b, MathWorks, USA). Various designs of auxetic structures following the procedures are visualized in Figure 1A(iv).

2.1.2. Numerical evaluations

We utilized FEA to evaluate effective strain fields within the complex auxetic structures generated by the aforementioned procedure. Abaqus software (Abaqus 2017,

Dassault Systèmes, USA) was used, with proper input files for the solver formatted via Matlab code used in the design generation. The mesh for the unit cell consisted of a 128×128 grid, matching the pixels, as depicted in Figure 1B(i). Considering the repetitive geometric characteristics of the auxetic unit cells, periodic boundary conditions were employed for corresponding boundary nodes, as depicted in Figure 1B(ii). The solid phase was considered to be linearly elastic, with material parameters of 1,144.51 MPa for Young's modulus (E) and 0.38 for Poisson's ratio (ν). The strain field results were extracted by simulating the structure's response to tensile loading, considering plane stress conditions for two-dimensional analysis.

On the calculation of the simulation, the resulting three strain fields: ε_{xx} , ε_{yy} , and ε_{xy} were extracted and used to calculate effective strain fields as follows¹¹ (Equation V):

$$\varepsilon_{\text{equiv}} = \frac{2}{3} \left[\varepsilon_{xx}^2 + \varepsilon_{yy}^2 + \varepsilon_{zz}^2 - \varepsilon_{xx}\varepsilon_{yy} - \varepsilon_{yy}\varepsilon_{zz} - \varepsilon_{zz}\varepsilon_{xx} + 3\varepsilon_{xy}^2 \right]^{\frac{1}{2}}, \quad (\text{V})$$

Where $\varepsilon_{zz} = -\frac{\nu}{1-\nu}(\varepsilon_{xx} + \varepsilon_{yy})$ from a plane stress condition. Furthermore, to access the NPR characteristic of the designed auxetic structures, Poisson's ratio for the overall unit cell was calculated as the ratio between average longitudinal and transverse strains as follows (Equation VI):

$$\nu_{\text{unit cell}} = -\frac{\overline{\varepsilon}_{xx}}{\overline{\varepsilon}_{yy}}, \quad (\text{VI})$$

Where $\overline{(\cdot)}$ denotes the volume average over the unit cell. Here, the y -direction is the loading direction. Therefore, $\overline{\varepsilon}_{yy}$ is the average longitudinal strain, whereas $\overline{\varepsilon}_{xx}$ being the average transverse strain.

Through the process, two types of outputs were obtained for each auxetic structure design: (i) the effective strain fields stored as a 128×128 array and (ii) the structural Poisson's ratio value, which is a single scalar. In the next section, we demonstrate the data-driven model architecture employed to accurately predict the effective strain fields. The dataset formulated by extracting those outputs for N designs is depicted in Figure 1B(iii).

2.2. DL model architecture

This study utilized a modified MNet DL architecture³⁰ for the effective mapping of auxetic structure configurations to their respective effective strain fields, as depicted in Figure 1C. The model was equipped with an encoder-decoder framework, deploying a multi-kernel approach.^{30,40} By integrating a separable convolution technique⁴¹ within its density-populated multi-kernel block, the model was capable of detecting intricate patterns and predicting effective strain field attributes.

The 128×128 pixelized auxetic structure design, with

"1" indicating solid phase and "0" representing void, was used as an input to the model. The encoder utilized multi-scale kernels sized at 3×3 , 6×6 , and 9×9 to analyze spatial correlations and connectivity among the solid phases within the structure. This process allowed the identification of diverse auxetic patterns with elevated accuracy by leveraging information from multiple kernels. Specifically, small-sized kernels were adept at detecting immediate connectivity, whereas large-sized kernels can capture broader structural correlations across the grid.

To further enhance the computational efficiency of the model, convolutional feature maps were normalized based on the number of multi-kernels applied. These feature maps from fusion layers act as inputs for subsequent layers, where precise 1×1 pointwise convolution operations were employed to preserve essential structural information.⁴² Within the down-sampling layers, the 2×2 max-pooling operation reduces the spatial dimensions of the feature map while preserving critical structural details. The model introduced a custom transpose convolution technique to aid in the reconstruction of compacted feature maps, establishing a direct connection with the corresponding feature maps in the finer layers of the encoder.

Notably, the modified MNet introduced a separable convolution approach to address the checkerboard issue, a common artifact in conventional transpose convolution operations. The issue, characterized by distinct patterns in CNN's output feature maps, is effectively mitigated by adapting the separable approach.⁴¹ Mitigating checkerboard issues is essential for accurate prediction of the effective strain fields.³⁸ The training of the DL model was performed on a personal desktop computer equipped with a graphic processing unit (GeForce RTX4090, Nvidia, USA).

2.3. Three-dimensional printing and testing of ML composite specimen

2.3.1. Materials

The ML particle utilized in this study is composed of strontium aluminate (SAOED; SrAl_2O_4 ; Eu^{2+} , Dy^{3+}) with an average size of $10 \mu\text{m}$ (GSS-300FF, Nemoto and Co., Japan), which emits green photons on stressing due to the ML effect (Figure 2A). For the 3D printing of ML-enriched composites, we utilized a photocurable polymer resin (AMB Med-10, 3D Systems, USA) as the matrix. The resin was chosen for its transparency (ISO 10993-5 certified) to facilitate the visibility of ML particle emissions.

2.3.2. DLP-3D printing

To evaluate the mechanical and photonic characteristics of ML composites under tensile loading, we fabricated the composite specimens in dog-bone shape with the DLP 3D

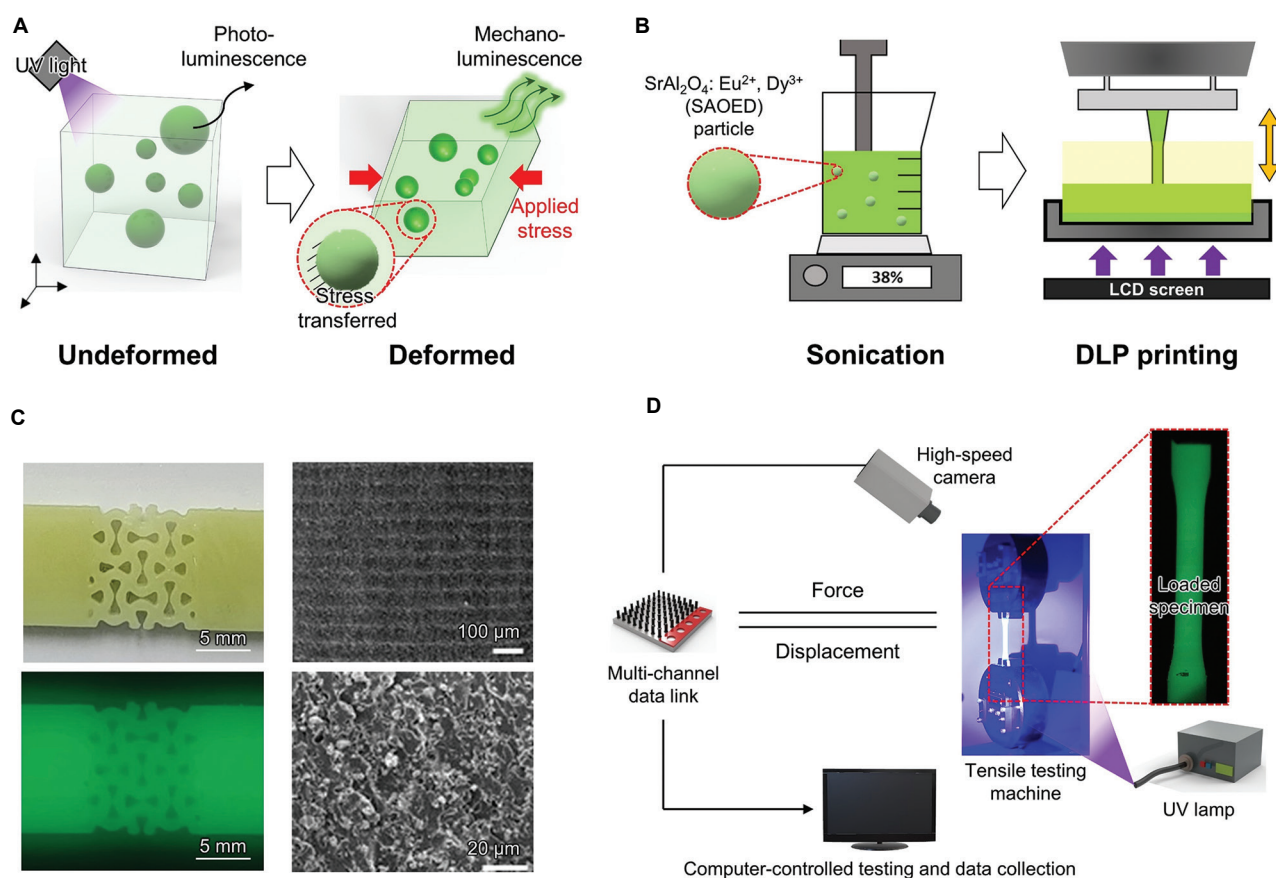


Figure 2. Mechanoluminescent (ML) composite specimen and its fabrication and testing. (A) Schematic of photo-luminescence of SAOED particle induced by ultraviolet charging and ML emission induced by deformation. (B) Schematic of digital light processing-3D printing process with resin-particle mixture preparation. (C) Image of fabricated ML composite specimen and scanning electron microscopy (SEM) image of the specimen surface. (D) Schematics of testing setup for tensile loading and ML intensity.

printing method (Figure 2B). The SAOED powder was mixed with resin with a planetary centrifugal mixer (MSK-300, Tmaxcn Co., China) and ceramic balls. The mixing process was conducted 3 times: 1 min at 3,354g, followed by 4 min at 13,416g each, ensuring uniform dispersion of particles. To minimize the phase separation within the resin, 1 h of ultrasonication was performed (VCX-750, Sonics and Materials Inc., USA; at 38% energy setup). Subsequently, the prepared resin-particle mixture was utilized in a DLP printer (Standalone Model 4, 3D Systems, USA), and tensile testing was conducted for the printed dog-bone specimen, which is fabricated according to ASTM D638 standards.⁴³ The DLP printing was performed with a layer thickness of 50 μm and 3 mm for the printing part and support layers, respectively, with a cure depth of 175 μm (Figure 2C). After printing, the specimens underwent post-curing in an ultraviolet (UV) box (3D Systems) for 5 min for complete curing.

2.3.3. Tensile testing and ML analysis

To validate numerical and data-driven predictions

and demonstrate the applicability of ML phenomena in analyzing effective strain fields within loaded ML composite specimens, the printed specimens were tested with a universal testing machine (AGS-X, Shimadzu, Japan) with a fixed strain rate of 0.1%/min and a data sampling rate of 100 Hz. To measure ML intensity and identify regions with strain concentration within the specimen, each specimen was exposed to UV light for 1 min using a UV lamp (Inno-Cure 5000, Lichtzen Co., Republic of Korea) with a wavelength range of 250 – 450 nm before tensile testing. Subsequently, the specimens were placed in a dark room for 2 min to mitigate the afterglow effect. To image the luminescence distribution emitted by ML particles upon straining, a high-resolution digital camera (EOS R7, Canon, Japan) was used with a sampling frequency of 10 Hz. The experimental setup for capturing ML phenomena is depicted in Figure 2D.

2.3.4. DIC method

The DIC method calculates strain on the specimen surface

by capturing the difference in distance between specific points on the specimen during deformation. The process requires prior artificial patterning on the specimen surface and algorithms to analyze images and calculate distances. In this study, to investigate the strain distribution within the specimen and map ML intensity to equivalent strain, DIC measurement was utilized during tensile testing. Strain measurement was conducted using an algorithm provided by a commercial program (Aramis, Gesellschaft für Optische Messtechnik mbH, Germany), which provided a 0.005% error. The experimental setup included a light-emitting diode lighting system and two six-megapixel charge-coupled device (CCD) cameras, calibrated to measure a region of interest (ROI) sized $30 \times 24 \text{ mm}^2$ to acquire high-resolution images. Speckle patterns were randomly generated on the specimen surfaces using ceramic spray (SF 7900, Loctite, Germany) for the calculation of strain. Images were captured at a frequency of 3 Hz by the two CCD cameras during the tensile test. Strain distribution in the 3D-printed specimen was analyzed at multiple subsets in the ROI, utilizing normalized correlation coefficients to extract accurate strain data. Advanced filtering algorithms provided by the Aramis software were applied to minimize noise and eliminate outlier peak data, ensuring data integrity).

3. Results and discussion

3.1. Prediction of DL model

The predictive performance of the DL architecture utilizing the modified MNet on the effective strain field of various auxetic structures is presented here. Despite training the model with a relatively limited dataset of 487 samples, the architecture effectively captured the target field with the aid of multi-kernels. The dataset was split into 390 samples for training and 97 samples for testing. To mitigate the variation in model performance due to different dataset splits, we utilized k -fold cross-validation using 5 folds

($k = 5$). The average validation loss of the effective strain field was $9.464e^{-5}$. The evaluated performance metrics demonstrate that the data-driven approach is capable of accurately predicting effective strain fields, with a computation speed approximately 10^4 times faster than FEA (Figure 3A). The training process for each model took 3,456 s (approximately 1 h) on a desktop computer equipped with an NVIDIA GeForce RTX 4090 GPU. This approach also effectively prevented the checkerboard issue inherent in conventional CNN-based architectures. Thus, the DL architecture holds promise as an efficient alternative to conventional FEA for evaluating auxetic structures. The comparison of finite element method (FEM) and DL predictions of the effective strain field and their relative errors is visualized in Figure 3B. Figure S1 provides a comparison of three randomly selected configurations, demonstrating the high accuracy of the data-driven model.

3.2. Evaluation of 3D-printed ML composite specimen

In this section, we evaluate and analyze the luminescence behavior of 3D-printed ML composite specimens by measuring and quantifying light intensity upon loading. We demonstrate that the ML-based non-contact evaluation technique can capture the strain field measured by DIC, a widely adopted conventional technique.

3.2.1. Consistency of ML intensity and DIC measured strain field

This section addresses the applicability of ML intensity change as an alternative to conventional DIC techniques through the evaluation of tensile test specimens following ASTM D638.

In the 3D-printed dog-bone specimen of ML composite, four subset areas were set to assess the consistency of the DIC measured strain field and ML intensity (Figure 4; top

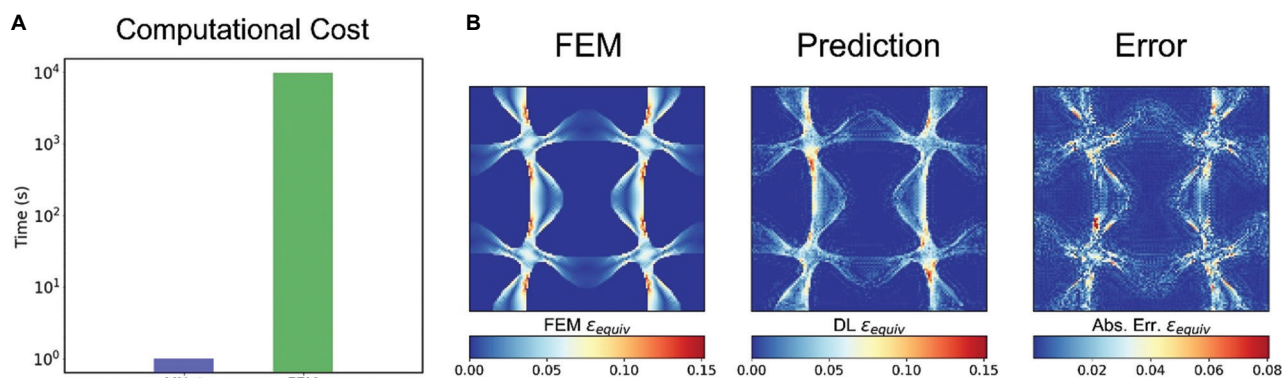


Figure 3. Prediction results of the deep learning (DL) model for random configuration. (A) Computation time comparison of the finite element method (FEM) and MNet from the DL model. (B) Results of the effective strain field by the DL model and FEM a 0.1% tensile condition.

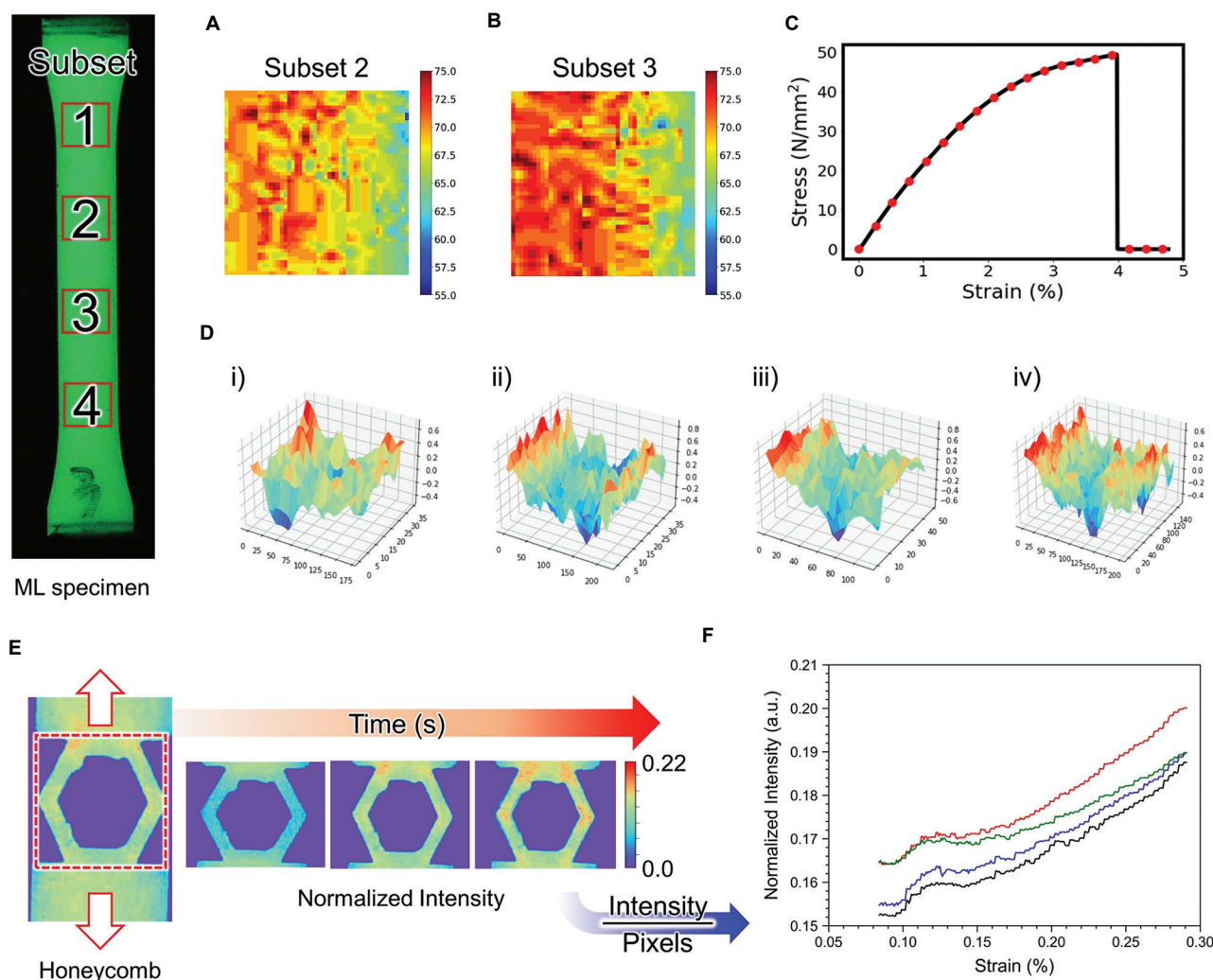


Figure 4. Assessment of the capability of a 3D-printed composite specimen compared with the digital image correlation technique. (A) The variations in the local intensity pattern of the composite specimen at 0.1% strain in Subset 2. (B) The variations in the local intensity pattern of the composite specimen at 0.1% strain in Subset 3. (C) Stress-strain curve of the composite dog-bone specimen. (D) The 3D plot illustrates the distribution of cross-correlation coefficient values within each subset area. (E) Mechanoluminescent intensity evolution under tensile testing of honeycomb structure. (F) Normalized intensity versus strain curve of tensile testing of the honeycomb structure.

left corner). Figures 4A and B visualize the light intensity distribution of Subsets 2 and 3, respectively, at 1% tensile strain (Figure 4C). Differences in intensity patterns between the two regions were observed, similar to typical DIC measurements, suggesting that the ML technique can address the intricate strain field within the tensile specimen.

The DIC technique utilizes a normalized cross-correlation coefficient (NCC) to determine paired pixels for subsequent images.¹¹ The pattern similarity can be assessed through the maximum NCC values, ranging from 0 to 1, where values closer to one indicate high similarity. The NCC was computed utilizing a calculation algorithm, which can be found in Yoo and Han (2009).⁴⁴ In this study,

four reference image sets and corresponding deformed images (50 × 50 pixels) were analyzed. The NCC values for Subsets 1 to 4 were 0.48, 0.88, 0.92, and 0.79, respectively (Figure 4D [i-iv]). These results indicate effective analysis of both reference and deformed images, allowing reliable position tracking.¹¹ Moreover, the presence of ML light emission during tensile testing does not interfere with the DIC algorithm's ability to analyze NCC.¹¹

3.2.2. Analysis of ML intensity

In addition to NCC, pixel intensity values allow for the analysis of light intensity fields over time during tensile testing.⁴⁵ To verify the ML intensity-effective strain relationship, we further evaluated the more complex

honeycomb structure. The structure is widely adopted in sensor applications for its lightweight and efficient stress distribution.⁴⁶ Considering that the structure has been extensively analyzed and documented in the literature, it provides a robust foundation for understanding and validating the ML measurement technique. A honeycomb structure with a thickness of 0.75 mm and a length of 3 mm was used (Figure 4E).

It is important to note that the 3D-printed ML specimens emit light not only due to luminescence induced by external mechanical stimuli but also due to an afterglow effect with sustained emission.⁴⁵ To ensure an accurate assessment of light intensity and achieve high reproducibility with a high signal-to-noise ratio, the tensile tests were conducted after the emission of the specimens had saturated, which occurred 2 min after UV treatment.

Figure 4E demonstrates an intuitive trend of high intensity in localized strain regions, corresponding to areas of high effective strain. The increase in light intensity over time reflects the increased effective strain with increasing loading. By analyzing the intensity during tension, the normalized ML intensity is quantified as a function of global strain, as depicted in Figure 4F. Specifically, at a global strain of 0.3%, the maximum values at the four ROIs of the specimen exhibit intensity differences, as demonstrated in Figure S2. These quantified intensities allow us to approximate the values of the local strain field. Therefore, recognizing local strain field patterns is possible through the analysis of ML intensity variations.

3.2.3. Direct mapping of ML intensity to effective strain

The ML image intensity field contains scalar information at the pixel level, whereas DIC measurement typically provides vector information of strain fields. To investigate these two datasets, we converted the vector information of

DIC strain fields into scalar values using Equation 5. This conversion aligns with the output field dataset shown in Figure 1B [iii]. For calibration between effective strain and ML intensity, bicubic interpolation was implemented,⁴⁷ using four subset windows of 25×25 pixels.

The mapping result between effective strain and ML intensity is depicted in Figure 5A. A strong linear correlation is observed, represented by Equation VII:

$$(I_{ML} = 137 \times \varepsilon_{equiv}) \quad (VII)$$

where I_{ML} denotes the ML intensity. This confirms the feasibility of linear regression, suggesting that the ML response of the specimen is linear and proportional to the effective strain.

This approach enables the quantification and calibration of ML intensity, facilitating direct analysis of equivalent strain fields using ML intensity information. As depicted in Figure 5B, the effective strain field measured from DIC (Figure 5B[i]) and obtained via transformed ML intensity values (Figure 5B[ii]) displays similar patterns with increasing global strain. The results indicate consistency in the effective strain fields obtained by the two approaches.

Mapping the measured ML intensity to effective strain fields offers two primary advantages. Firstly, it allows a straightforward examination of the correlation between the two parameters through direct data processing. Secondly, utilizing effective strain fields, which are scalar fields, enhances data accuracy compared to utilizing vector field quantities. This method is applicable to specimens with complex auxetic structures, as demonstrated in the following section.

3.3. Validation of DL prediction with ML-aided characterization

The effective strain fields predicted by the DL model, as

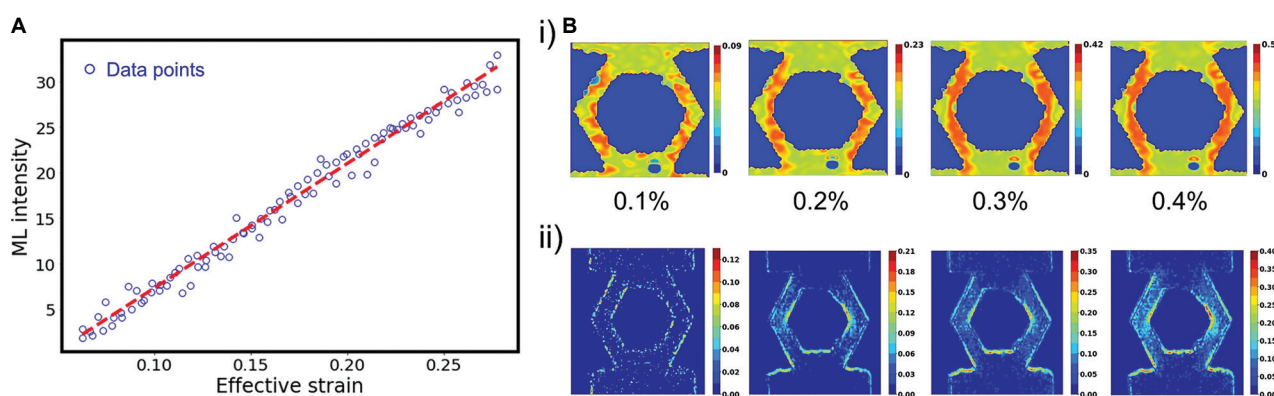





Figure 5. Relationship between mechanoluminescent (ML) intensity and effective strain and visualization in a honeycomb structure. (A) Calibration is derived from a linear regression of ML intensity with effective strain. (B) Comparison of effective strain measured by (i) digital image correlation and (ii) calculated by ML transformed during the tensile test of honeycomb structure.

Table 1. Design parameters of the auxetic structure

Design	Unit cell	Design variable			
		ϕ	τ	x	y
1		0.066	0.211	0.154	0.102
2		0.070	0.169	0.120	0.169
3		0.132	0.215	0.294	0.141

presented in Section 3.1, were evaluated against the effective strain obtained via ML intensity analysis. For the experimental analysis of auxetic structures, the three configurations and design parameters presented in Table 1 were 3D-printed and subjected to tensile testing. Considering that the printed specimens demonstrated a linear regime within 0.1% of strain (in global stress-strain behavior (Figure S3), the analysis was conducted at the same strain level.

Figure 6 presents the strain fields of the three auxetic designs calculated via FEA (convergence analysis is presented in Figure S4, and the results for pixelized cells and the number of elements per pixel under various conditions are presented in Tables S1 and S2), predicted with the DL model, and calculated from the ML-aided characterization. The selected structures were chosen arbitrarily among designs possessing NPR characteristics, with NPR values characterized by the DL model. The results demonstrate that comparable strain field patterns are obtainable from the three analyses. Specifically, the ML-aided characterizations

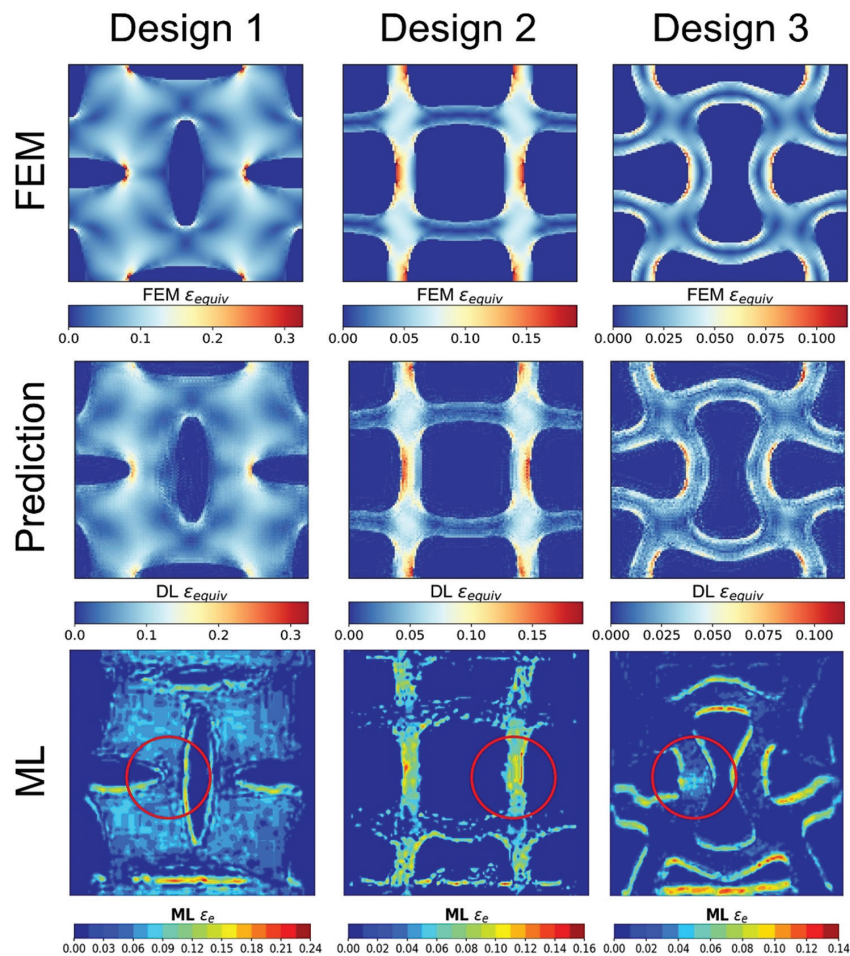


Figure 6. Prediction of deep learning (DL) model and experimental validation. Finite element method- and DL-predicted effective strain field, and mechanoluminescent-transformed result at 0.1% tensile strain condition

revealed pronounced strain values in the areas denoted by red circles. These locations are consistent with those predicted by FEM and the DL model. Consequently, the Mnet provides accurate predictions of effective strain fields for diverse auxetic designs, matching well with both numerical analysis and experimental observations.

However, certain discrepancies still exist between FEM predictions and ML measurements. Two potential causes are hypothesized:

- i. Material property deviation: Specimens fabricated through additive manufacturing may have limited particle uniformity, whereas FEM assumes perfect homogeneity, potentially leading to differences in intensity distribution.
- ii. Precision of fabrication: The precision of the 3D printer may be limited, with DLP-printed specimens exhibiting weakened interlayer adhesion, introducing variation in mechanical properties. FEM analysis, on the other hand, assumes perfect bonding with every portion of the structure.

Addressing these potential issues could improve the agreement between predicted and measured values.

An investigation into the relation between normalized intensity and structural Poisson's ratio was conducted for the three designs. The results, shown in Figure S5, indicate that auxetic structures with high NPR exhibit high intensity at the same global deformation. This trend is due to increased rotational deformation within the unit cell in high NPR structures, leading to increased localized strain and thus high-intensity values. Given the favored NPR characteristics of auxetic structures in design applications, the ML method demonstrates high sensitivity for the designs. Therefore, future designs of various auxetic structures could benefit from the application of ML methods for real-time monitoring and effective verification of structural reliability.

4. Conclusion

This study presented a comprehensive framework for predicting the effective strain in auxetic structures, validated through ML-aided non-contact reliability evaluation of 3D-printed specimens. The findings underscore the potential of ML-based structural reliability assessments as cost-effective and deployable solutions for SHM applications, particularly for intricate designs such as auxetic structures.

The key contributions of the study include:

- i. Unique parametrization with Bézier curves: The use of Bézier curves for parametrizing auxetic structures ensured smooth surfaces, efficiently avoiding stress concentrations associated with sharp corners. This technique enhances the overall structural integrity

and reliability of the designs.

- ii. Advanced DL architecture: To address the high computational costs associated with evaluating a large design space of auxetic structures, an advanced DL architecture, the modified MNet, was employed. This DL model achieved over 90% accuracy and demonstrated evaluation speed approximately 10^4 times faster than FEA, using a relatively limited dataset of 387 training samples.
- iii. Experimental validation: The model's predictions were validated using experimental techniques incorporating ML-aided non-contact evaluation. The results showed good agreement, particularly in areas with high-stress concentrations. This validation underscores the effectiveness of the data-driven model in accurately predicting strain fields.
- iv. Comparison with the DIC technique: The ML-based structural reliability evaluation technique was calibrated and validated against the DIC technique. While DIC provides accurate strain field assessments, its high cost and complex setup limit its applicability. The ML method, through careful mapping between ML intensity and strain fields, demonstrated excellent agreement with DIC measurements, highlighting its potential as a cost-effective SHM technique.
- v. Practical applicability: The study demonstrates the feasibility of simultaneous prediction, fabrication, and direct evaluation of structural reliability in various intricate structures, exemplified by auxetic metamaterial designs. The proposed ML methodology shows significant potential for practical applications requiring high sensitivity to deformation, including aircraft design, pipe monitoring, and sensors.

In conclusion, the research provides a robust framework for effective strain prediction and structural reliability assessment using ML-based methods. The results highlight the practicality and efficiency of these techniques in real-world applications, paving the way for advanced SHM systems that are both cost-effective and highly sensitive to structural deformations.

Acknowledgments

Not applicable.

Funding

This work was financially supported by the National Research Foundation of Korea (NRF) (RS-2023-00222166).

Conflict of interest

Seunghwa Ryu is an Editorial Board Member of this journal, but was not in any way involved in the editorial

and peer-review process conducted for this paper, directly or indirectly. Separately, other authors declared that they have no known competing financial interests or personal relationships that could have influenced the work reported in this paper.

Author contributions

Conceptualization: Junheui Jo, Hugon Lee

Investigation: Junheui Jo

Methodology: Junheui Jo, Sukheon Kang, Minwoo Park, Chang-Yeon Gu

Supervision: Taek-Soo Kim, Seunghwa Ryu

Writing – original draft: Junheui Jo, Hugon Lee

Writing – review & editing: Junheui Jo, Hugon Lee, Sukheon Kang, Minwoo Park, Seunghwa Ryu

Ethics approval and consent to participate

Not applicable.

Consent for publication

Not applicable.

Availability of data

Data used in this work are available from the corresponding author on reasonable request.

References

1. Zhang XY, Ren X, Zhang Y, Xie YM. A novel auxetic metamaterial with enhanced mechanical properties and tunable auxeticity. *Thin Walled Struct.* 2022;174:109162. doi: 10.1016/j.tws.2022.109162
2. Xin X, Liu L, Liu Y, Leng J. 4D printing auxetic metamaterials with tunable, programmable, and reconfigurable mechanical properties. *Adv Funct Mater.* 2020;30(43):2004226. doi: 10.1002/adfm.202004226
3. Cheng X, Zhang Y, Ren X, et al. Design and mechanical characteristics of auxetic metamaterial with tunable stiffness. *Int J Mech Sci.* 2022;223:107286. doi: 10.1016/j.ijmecsci.2022.107286
4. Ilani MA, Khoshnevisan M. Powder mixed-electrical discharge machining (EDM) with the electrode is made by fused deposition modeling (FDM) at Ti-6Al-4V machining procedure. *Multiscale Multidiscip Model Exp Des.* 2020;3(3):173-186. doi: 10.1007/s41939-020-00070-6
5. Wang Z, Luan C, Liao G, Liu J, Yao X, Fu J. Progress in auxetic mechanical metamaterials: Structures, characteristics, manufacturing methods, and applications. *Adv Eng Mater.* 2020;22(10):2000312. doi: 10.1002/adem.202000312
6. Yu X, Zhou J, Liang H, Jiang Z, Wu L. Mechanical metamaterials associated with stiffness, rigidity and compressibility: A brief review. *Prog Mater Sci.* 2018;94:114-173. doi: 10.1016/j.pmatsci.2017.12.003
7. Evans KE, Alderson A. Auxetic materials: Functional materials and structures from lateral thinking! *Adv Mater.* 2000;12(9):617-628. doi: 10.1002/(SICI)1521-4095(200005)12:9%3C617::AID-ADMA617%3E3.0.CO;2-3
8. Li Y, Luo S, Yang MC, Liang R, Zeng C. Poisson ratio and piezoresistive sensing: A New route to high-performance 3D flexible and stretchable sensors of multimodal sensing capability. *Adv Funct Mater.* 2016;26(17):2900-2908. doi: 10.1002/adfm.201505070
9. Zhai X, Gao J, Liao H, Kirk CD, Balogun YA, Chen WW. Mechanical behaviors of auxetic polyurethane foam at quasi-static, intermediate and high strain rates. *Int J Impact Eng.* 2019;129:112-118. doi: 10.1016/j.ijimpeng.2019.03.002
10. Grima JN, Evans KE. Auxetic behavior from rotating squares. *J Mater Sci Lett.* 2000;19:1563-1565. doi: 10.1023/A:1006781224002
11. Tretiakov KV. Negative poisson's ratio of two-dimensional hard cyclic tetramers. *J Non Cryst Solids.* 2009;355(24-27):1435-1438. doi: 10.1016/j.jnoncrysol.2009.05.043
12. Shin HG, Timilsina S, Sohn KS, Kim JS. Digital image correlation compatible mechanoluminescent skin for structural health monitoring. *Adv Sci.* 2022;9(11):2105889. doi: 10.1002/advs.202105889
13. Feng A, Smet PF. A review of mechanoluminescence in inorganic solids: Compounds, mechanisms, models and applications. *Materials (Basel).* 2018;11(4):484. doi: 10.3390/ma11040484
14. Timilsina S, Kim JS, Kim J, Kim GW. Review of state-of-the-art sensor applications using mechanoluminescence microparticles. *Int J Precis Eng Manuf.* 2016;17(9):1237-1247. doi: 10.1007/s12541-016-0149-y
15. Zhang JC, Wang X, Marriott G, Xu CN. Trap-controlled mechanoluminescent materials. *Prog Mater Sci.* 2019;103:678-742. doi: 10.1016/j.pmatsci.2019.02.001
16. Ni S, Zhu H, Neuzil P, Yobas L. A SiN microcalorimeter and a non-contact precision method of temperature calibration. *J Microelectromech Syst.* 2020;29(5):1103-1105.

- doi: 10.1109/JMEMS.2020.3008867
17. Ennaceur C, Laksmi A, Hervé C, Cherfaoui M. Monitoring crack growth in pressure vessel steels by the acoustic emission technique and the method of potential difference. *Int J Press Vessels Piping*. 2006;83(3):197-204.
doi: 10.1016/j.ijpvp.2005.12.004
 18. Wang JY, Guo JY. Damage investigation of ultra high performance concrete under direct tensile test using acoustic emission techniques. *Cem Concr Compos*. 2018;88:17-28.
doi: 10.1016/j.cemconcomp.2018.01.007
 19. Wen TK, Yin CC. Crack detection in photovoltaic cells by interferometric analysis of electronic speckle patterns. *Sol Energy Mater Sol Cells*. 2012;98:216-223.
doi: 10.1016/j.solmat.2011.10.034
 20. Zarate EA, Custodio GE, Treviño-Palacios CG, Rodríguez-Vera R, Puga-Soberanes HJ. Defect detection in metals using electronic speckle pattern interferometry. *Sol Energy Mater Sol Cells*. 2005;88(2):217-225.
doi: 10.1016/j.solmat.2004.03.009
 21. Liang Z, Qin F, Zheng Y, Zhang Z, Cao W. Noncontact thermometry based on downconversion luminescence from Eu³⁺ doped LiNbO₃ single crystal. *Sens Actuators A Phys*. 2016;238:215-219.
doi: 10.1016/j.sna.2015.12.018
 22. Antić Ž, Damićanin MD, Prashanthi K, Jovanović D, Kuzman S, Thundat T. Pulsed laser deposited dysprosium-doped gadolinium–vanadate thin films for noncontact, self-referencing luminescence thermometry. *Adv Mater*. 2016;28(35):7745-7752.
doi: 10.1002/adma.201601176
 23. Schlothauer JC, Grabmayer K, Hintersteiner I, Wallner GM, Röder B. Non-destructive 2D-luminescence detection of EVA in aged PV modules: Correlation to calorimetric properties, additive distribution and a clue to aging parameters. *Sol Energy Mater Sol Cells*. 2017;159:307-317.
doi: 10.1016/j.solmat.2016.09.011
 24. Stepanova LV, Yakovleva EM. Asymptotic stress field in the vicinity of a mixed-mode crack under plane stress conditions for a power-law hardening material. *J Mech Mater Struct*. 2015;10(3):367-393.
doi: 10.2140/jomms.2015.10.367
 25. Berto F, Lazzarin P. Recent developments in brittle and quasi-brittle failure assessment of engineering materials by means of local approaches. *Mater Sci Eng R Rep*. 2014;75(1):1-48
doi: 10.1016/j.mser.2013.11.001
 26. Altenbach H, Hitzler L, Johlitz M, Merkel M, Öchsner A, editors. *Lectures Notes on Advanced Structured Materials 2*. Vol. 203. Switzerland: Springer Nature; 2024.
doi: 10.1007/978-3-031-49043-9
 27. Abueidda DW, Almasri M, Ammourah R, Ravaioli U, Jasiuk IM, Sobh NA. Prediction and optimization of mechanical properties of composites using convolutional neural networks. *Compos Struct*. 2019;227:111264.
doi: 10.1016/j.compstruct.2019.111264
 28. Yang Z, Yabansu YC, Jha D, *et al*. Establishing structure-property localization linkages for elastic deformation of three-dimensional high contrast composites using deep learning approaches. *Acta Mater*. 2019;166:335-345.
doi: 10.1016/j.actamat.2018.12.045
 29. Fu T, Monaco F, Li J, *et al*. Deep-learning-enabled crack detection and analysis in commercial lithium-ion battery cathodes. *Adv Funct Mater*. 2022;32(39):2203070.
doi: 10.1002/adfm.202203070
 30. Park D, Park M, Ryu S. Expanding design spaces in digital composite materials: A multi-input deep learning approach enhanced by transfer learning and multi-kernel network. *Adv Theory Simul*. 2023;6(11):2300465.
doi: 10.1002/adts.202300465
 31. Ammasai Sengodan G. Prediction of two-phase composite microstructure properties through deep learning of reduced dimensional structure-response data. *Compos B Eng*. 2021;225:109282.
doi: 10.1016/j.compositesb.2021.109282
 32. Lee J, Park D, Lee M, *et al*. Machine learning-based inverse design methods considering data characteristics and design space size in materials design and manufacturing: A review. *Mater Horiz*. 2023;10(12):5436-5456.
doi: 10.1039/d3mh00039g
 33. Tan RK, Zhang NL, Ye W. A deep learning-based method for the design of microstructural materials. *Struct Multidiscip Optim*. 2020;61(4):1417-1438.
doi: 10.1007/s00158-019-02424-2
 34. Li HN, Ren L, Jia ZG, Yi TH, Li DS. State-of-the-art in structural health monitoring of large and complex civil infrastructures. *J Civil Struct Health Monit*. 2016;6(1):3-16.
doi: 10.1007/s13349-015-0108-9
 35. Diamanti K, Soutis C. Structural health monitoring techniques for aircraft composite structures. *Prog Aerosp Sci*. 2010;46(8):342-352.
doi: 10.1016/j.paerosci.2010.05.001
 36. Ye XW, Su YH, Han JP. Structural health monitoring of civil infrastructure using optical fiber sensing technology: A comprehensive review. *Sci World J*. 2014;2014:652329.
doi: 10.1155/2014/652329
 37. Li C, He Q, Wang Y, *et al*. Highly robust and soft biohybrid mechanoluminescence for optical signaling and

- illumination. *Nat Commun.* 2022;13(1):3914.
doi: 10.1038/s41467-022-31705-6
38. Song H, Park E, Kim HJ, *et al.* Free-form optimization of pattern shape for improving mechanical characteristics of a concentric tube. *Mater Des.* 2023;230:111974.
doi: 10.1016/j.matdes.2023.111974
39. Lee S, Choi W, Park JW, *et al.* Machine learning-enabled development of high performance gradient-index phononic crystals for energy focusing and harvesting. *Nano Energy.* 2022;103:107846.
doi: 10.1016/j.nanoen.2022.107846
40. Park D, Jung J, Gu GX, Ryu S. A generalizable and interpretable deep learning model to improve the prediction accuracy of strain fields in grid composites. *Mater Des.* 2022;223:111192.
doi: 10.1016/j.matdes.2022.111192
41. Luján-García JE, Yáñez-Márquez C, Villuendas-Rey Y, Camacho-Nieto O. A transfer learning method for pneumonia classification and visualization. *Appl Sci (Basel).* 2020;10(8):2908.
doi: 10.3390/APP10082908
42. Reddy CKA, Dubey H, Gopal V, *et al.* ICASSP 2021 Deep Noise Suppression Challenge. In: *ICASSP 2021 - 2021 IEEE International Conference on Acoustics, Speech and Signal Processing (ICASSP).* IEEE; 2021:6623-6627.
doi: 10.1109/icassp39728.2021.9415105
43. Laureto JJ, Pearce JM. Anisotropic mechanical property variance between ASTM D638-14 type I and type IV fused filament fabricated specimens. *Polym Test.* 2018;68:294-301.
doi: 10.1016/j.polymertesting.2018.04.029
44. Yoo JC, Han TH. Fast normalized cross-correlation. *Circuits Syst Signal Process.* 2009;28(6):819-843.
doi: 10.1007/s00034-009-9130-7
45. Song H, Timilsina S, Jung J, Kim TS, Ryu S. Improving the sensitivity of the mechanoluminescence composite through functionalization for structural health monitoring. *ACS Appl Mater Interfaces.* 2022;14(26):30205-30215.
doi: 10.1021/acsami.2c07286
46. Qi C, Jiang F, Yang S. Advanced honeycomb designs for improving mechanical properties: A review. *Compos B Eng.* 2021;227:109393.
doi: 10.1016/j.compositesb.2021.109393
47. Han D. Comparison of Commonly Used Image Interpolation Methods. In: *Proceedings of the 2nd International Conference on Computer Science and Electronics Engineering (ICCSEE 2013).* Atlantis Press; 2013:1556-1559.
doi: 10.2991/iccsee.2013.391